Journal of Renewable Materials

Tech Science Press

https://doi.org/10.32604/jrm.2026.02026-0022

ARTICLE

Synergistic Effect of Low-Concentration $ZnCl_2$-Activated Bio-Carbon from Red Suren Leaves with Hierarchical Pore Structure and Self-Doping for High-Performance Supercapacitor Applications

Erman Taer[1,*], Novi Yanti[1], Asmarwati[1], Apriwandi[1], Abrar Ismardi[2], Indra Wahyudhin Fathona[2], Memoria Rosi[2], Bidayatul Armynah[3], Dahlang Tahir[3], Ninis Hadi Haryanti[4], Suryajaya[4], Isnasyauqiah[5], Ida Usman[6], Julnaidi[7] and Rika Taslim[8,*]

[1]Department of Physics, University of Riau, Simpang Baru, Indonesia
[2]Department of Engineering Physics, School of Electrical Engineering, Telkom University, Bandung, Indonesia
[3]Department of Physics, Hasanuddin University, Makassar, Indonesia
[4]Department of Physics, University of Lambung Mangkurat, Banjarmasin, Indonesia
[5]Department of Chemical Engineering, University of Lambung Mangkurat, Banjarmasin, Indonesia
[6]Department of Physics, Haluoleo University, Kendari, Indonesia
[7]Department of Mechanical Engineering, Sekolah Tinggi Teknologi Pekanbaru, Pekanbaru, Indonesia
[8]Department of Industrial Engineering, Universitas Islam Negeri Sultan Syarif Kasim Riau, Simpang Baru, Indonesia

*Corresponding Authors: Erman Taer. Email: erman.taer@lecturer.unri.ac.id; Rika Taslim. Email: rikataslim@uin-suska.ac.id

Received: 11 February 2026; Accepted: 08 June 2026; Published: 26 August 2026

ABSTRACT: The promotion of bio-carbon for developing superior electrodes has become a trending topic in realising the practical application of supercapacitor devices. This study aimed to prepare porous carbon (PC) with a taproot fiber-like nanostructure that was decorated with self-doped oxygen. The waste of red suren leaves (RSL) was further treated using a direct heating method with the catalyst effect of $ZnCl_2$ (0.3, 0.5, and 0.7 M) in an N_2/CO_2 environment at 850°C, being examined. The results showed that RSL@PC-0.5 exhibited the best amorphous carbon structure (FWHM = 0.105° and 0.182°). The specific surface area (SSA = 495.31 m^2/g) and the combination of hierarchical nanostructure with abundant multi-level pores (micro-mesopores) were supported by the appropriate presence of O (4.26%) heteroatoms. Oxygen within the carbon matrix enhanced the electrode-electrolyte interaction by adding active sites, thereby contributing additional pseudocapacitance. Furthermore, the electrochemical performance showed a high specific capacitance of 490 F/g at a current density of 1 A/g. The energy density and power density reached 62.93 Wh/kg and 156.67 W/kg, indicating the excellent electrochemical performance of the RSL@PC-0.5 material. This study presented a supercapacitor material derived from biomass, showing a new PC with O self-doped fiber nanostructures that could serve as a rational reference for the practical application of environmentally friendly energy storage.

KEYWORDS: Red-suren-leaves; porous carbon; multi_level_pores; self-doping; supercapacitor_energy_storage

1 Introduction

The transition to sustainable and stable storage technologies is essential for achieving the vision of "Welcome to the era of Electricity and global energy independence". In this context, supercapacitors have evolved as promising candidates for large-scale backup energy storage and conversion devices [1,2]. As a key development in carbon-free technology from renewable resources, supercapacitors offer advantages such as high-power delivery, rapid charge-discharge rates, long service life, and adaptability [3,4]. Based on the

electrode configuration, supercapacitors are included in energy storage in two thermal aspects. This device is equipped with supporting components that contribute to the transfer of charged ions influenced by the potential difference at the working electrode. However, supercapacitors have limitations in energy density and stability, which necessitate modifications to electrode components using nanostructured materials with significant advantages [5–7].

Nanostructured materials enhance supercapacitor performance in several manners [8]. The materials provide a large surface area with abundant active sites for charge storage, thereby improving capacitance. The excellent electrical conductivity accelerates electron transfer through efficient transport pathways, facilitated by micro-meso-macro pores with minimal internal resistance. The materials enable greater energy storage through EDLC and redox reaction mechanisms. Nanostructured substance offers superior mechanical and chemical stability, enhancing the durability of supercapacitors. Among carbon-based nanostructures, materials such as highly PC have shown promising results. PC possesses natural microporosity, making the material an excellent adsorbent medium that can be produced from organic sources. The effective adoption of organic waste for PC production has gained increasing interest due to its role in reducing environmental emissions [9]. Biomass sources such as lemongrass [10], Tannin [11], Seaweed [12], chestnut shells [13], and other organic waste have been successfully converted into PC through chemical and physical activation processes.

Biomass-derived nanostructures exhibit diverse morphologies, carbon nanofibers are particularly well-suited for supercapacitor electrodes due to the high surface area, excellent electrical conductivity, strong adsorption capacity, mechanical stability, efficient ion and molecule transport, and flexible structural design [14]. However, directly identifying nanofibers within materials is not straightforward, necessitating various fabrication methods [15]. Previous studies have reported different approaches where Chen et al., (2021) used electrospinning to obtain fiber-like nanostructures from sugarcane [16]. Saxena et al. (2024) further used hydrothermal treatment to produce nanofibers from Sisal material [17], while Lv et al. (2024) adopted sol-gel processing to obtain nanofibers from pineapple leaves [18]. Similarly, Jing et al. (2025) applied a template printing method to produce nanofiber structures from natural filter paper [19]. However, these methods are often complex, costly, and time-consuming for large-scale PC production.

This study explores an alternative method by selecting aromatic biomass from *Toona sinensis* leaves (red suren leaves, RSL) as a precursor for fiber-like nanostructured materials. RSL are rich in organic polymers such as cellulose, hemicellulose, and lignin, which provide an excellent framework for nanofiber formation [20,21]. Cellulose, which is the main structural component of RSL cell walls, naturally forms fibrous microfibrils while hemicellulose and lignin act as protective matrices thermally modified into nanofibers [22]. The increasing interest in biomass waste valorisation enhances its economic and practical value, as biomass contains natural doping elements such as O, N, P, S, Zn, and B [23].

Specifically, oxygen doping has been identified as an effective strategy for improving the functional properties of PC, benefiting adsorption capacity, energy storage, and catalytic activity [24]. Biomass inherently contains oxygen functional groups, such as hydroxyl (-OH), carbonyl (-C=O), and carboxyl (-COOH), which enhance surface properties. Zinc doping can be introduced either naturally from biomass grown in mineral-rich environments or externally through chemical activation using $ZnCl_2$. $ZnCl_2$ has been recognised as a strong dehydrating agent, a porosity regulator, and a carbonisation temperature reducer, facilitating organic molecule breakdown to increase carbon purity and develop a porous structure. Zn and O doping significantly enhance the performance of supercapacitor electrodes by creating redox pseudocapacitance through the reversible redox reaction of Zn^{2+}/Zn^0 at the electrolyte-electrode interface, increasing active sites, and improving charge transfer kinetics [24]. However, O and Zn is a semiconductor compound with lower electron conductivity than carbon, if its amount is too much, it can reduce the performance of

EDLC [25]. Therefore, in this study, a review of the percentage content of $ZnCl_2$ catalyst material was carried out to produce a doped metal O and Zn, which is suitable for presenting pseudocapacitance. Furthermore, the choice of electrolyte plays a critical role in supercapacitor performance. H_2SO_4 is widely used due to its high ionic conductivity, compatibility with carbon electrodes, good thermal and electrochemical stability, as well as low cost [26]. During electrochemical operation, H_2SO_4 dissociates into H^{2+} cations and SO_4^{2-} anions, which adsorb onto the active carbon surface containing Zn. This doping further facilitates the spontaneous migration of H^{2+} ions, optimising ion diffusion pathways and increasing energy density as well as electrode lifespan through redox-enhanced charge storage [27].

In this study, RSL@PC-0.5 electrodes were produced from a novel material based on RSL waste PC as a sustainable precursor, and 0.5 M $ZnCl_2$ was adopted as a catalyst and Zn source. New material from RSL waste was used as a sustainable precursor, and $ZnCl_2$ was adopted as both a catalyst and a Zn source. The resulting material-Zn and O-doped natural taproot fiber-like nanofiber PC-was successfully synthesised through chemical impregnation, carbonisation, and physical activation. The optimised material prepared at 900°C with controlled catalyst loading exhibited a well-developed porous structure with a high total pore volume. Electrochemical characterisation performed using a two-electrode system showed excellent specific capacitance (490 F/g) and high energy density (62.93 Wh/kg), outlining the potential as an efficient and sustainable electrode material for supercapacitor applications.

2 Methodology

2.1 Carbon Preparation

Carbon material from RSL waste was prepared through a series of treatments. The preparation steps began with drying the RSL in the sun for 48 h, until a dry precursor with a yellow-brown color was obtained. The drying process was continued using a 110°C oven for 48 h, the aim being for more perfect drying, which was confirmed by the percentage of precursor mass shrinkage <6%. Then, as much as 300 g of sample was precarbonized using a vacuum oven at a temperature of 50°C–250°C for 2.5 h. The precarbonized sample was broken into particles by pounding it using a mortar and pestle until carbon particles were obtained <0.5 mm. The refining process was perfected using the help of collisions between steel balls and carbon particles in a vacuum tube for 20 h. Then, the carbon powder from ball milling was uniform in particle size in the size range <60 μm using a 250 mesh test sieve.

2.2 Synthesis of Porous Carbon

The synthesis scheme of RSL biomass waste to produce nano PC with a favorable structure, such as taproot fiber is illustrated in Fig. 1. The synthesis process begins with the preparation of a chemical activating agent solution by mixing ZnCl (0.3, 0.5, and 0.7) mol/L into 150 mL of distilled water. The dilution process of the activating agent was carried out using a set of hot plate and magnetic stirrer tools set at a temperature of 80°C and a stirring speed of 300 rpm for 1 h. Then, 30 g of carbon was added to each ZnCl solution and stirred again for 2 h. The chemically activated RSL carbon was dried in a drying oven at a temperature of 110°C for 5 h to dehydrate the remaining water content. The RSL carbon was molded into a monolithic solid coin to support the electrochemical analysis of the supercapacitor using a hydraulic press with a pressure equivalent to a mass of 8 t. Next, integrated pyrolysis of RSL samples was carried out in a furnace tube to produce PC with high purity and surface area. This process consisted of two main stages, namely carbonization and physical activation. Carbonization started with heating the sample under vacuum conditions using N_2 gas at 289°C for 1 h to maximize the evaporation of non-carbon elements. The temperature was then raised to 600°C at a controlled rate of 3°C/min under a continuous N_2 flow. Physical activation followed immediately, raising the temperature to 900°C while introducing CO_2 gas at a flow rate of 10°C/min. To optimize the pore

structure, the sample was held at this temperature for 2.5 h. The pyrolysis process concluded with cooling under vacuum conditions, followed by a second-density measurement. The PC coins were then neutralized to a pH of 7 through multiple washes with distilled water. The washing process was carried out by immersing the porous carbon electrode in 500 mL of distilled water, the distilled water was changed every 4 h, followed by measuring the electrode's pH. The washed samples were dried in an oven at 110°C for approximately 5 h. Once dried, the RSL-PC samples were prepared for physical and electrochemical characterization.

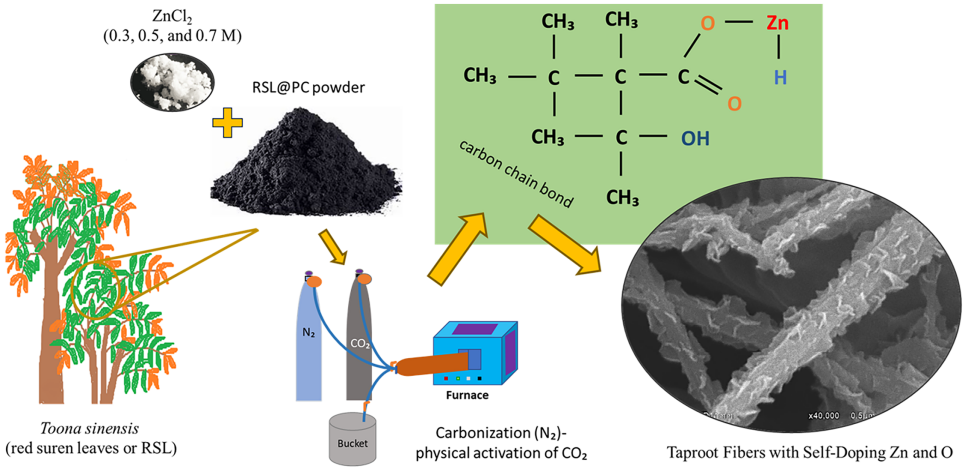

Figure 1: Schematic of preparation of RSL@PC-(x) precursor into natural Zn and O-doped nanostructured PC.

2.3 Structural Characterization and Electrochemical Measurements

The determination of the characteristics of RSL-activated carbon with a taproot-like pore structure was carried out through several analytical techniques. First, this analysis was carried out through the evaluation of the shrinkage of the mass size, diameter, and thickness of the carbon coin, which causes a change in mass and volume of the electrode before and after carbonization in an N_2 atmosphere and physical activation using CO_2 gas. Mathematically, density is determined using a simple equation: the mass of the electrode divided by its volume ($\rho = m/V$), where the mass is measured directly, while the volume is calculated based on the geometric dimensions of the monolithic (coin-shaped) electrode. Second, the determination of detailed information on the molecular analysis and crystallinity of carbon-based materials using Raman spectroscopy with a HORIBA Scientific tool and Labspec 6 software. Third, the crystallinity properties of the sample were tested through X-ray diffraction (XRD) energy characterization using a Shimadzu Merck type MAXima_X XRD 7000 No. BMN: 3.08.02.01.027. 1, PANalytical with a diffractometer system, Transmission Spinner PW3064/60 at the test point (10.01–99.97)° with a Cu-Ka light source ($\lambda = 1.54$). Fourth, the analysis of the shape and size of carbon particles in the morphological appearance was carried out by characterization of scanning electron microscopy using a Jeol JSM-IT200 vacuum brand instrument at room temperature of 24°C with secondary electron reflection. Fifth, the determination of the specific surface area (SSA), total pore volume, and pore size distribution of activated carbon through the Brunauer-Emmett Teller (BET) and Barrett-Joyner-Halanda (BJH) methods using the Quantachrome Nova 4200e instrument at a temperature of 300°C with a flow of 10°C/min for 60 min under the influence of absorbed nitrogen gas. The characterization of cyclic voltammetry (CV) and galvanostatic charge-discharge (GCD) was conducted as a fundamental analysis to determine the large storage capacity of RSL@PC when applied as a supercapacitor electrode. This test was carried out in a two-electrode system, assembled in a sandwich-like configuration with a specification diameter, thickness of 8, 0.2 mm and a working mass of 10 mg. This was separated by a

biomembrane from the eggshell in a sulfuric acid aqueous electrolyte. A 1 M H_2SO_4 solution was used as the source of electrically charged ions, which were stored in the pores of the carbon electrode due to the applied potential difference (0–1 V). The electric charge flow rate was set at 1 mV/s, and the current was maintained at 1 A to achieve maximum capacitance during CV and GCD testing.

The specific capacitance, energy density, and power density values for the CV and GCD method measurements are calculated based on the following equations.

$$C_{sp} = \frac{2I}{m \cdot s}, \text{ CV method} \qquad E = \frac{1}{2} C_{sp} \cdot (\Delta V)^2$$

$$C_{sp} = \frac{2I \cdot \Delta t}{m \cdot \Delta V}, \text{ GCD method} \quad P = \frac{E}{\Delta t}$$

where is,

$\bar{I}$ = average current Δt = charging-discharging time m_{single} = active mass of one electrode

s = scan rate (V/s) ΔV = electric potential difference

3 Results and Discussion

3.1 Density Analysis

The density analysis was related to the physical structure of the RSL@PC(x) electrode, as shown in Fig. 2a. RSL@PC-0.3, RSL@PC-0.5, and RSL@PC-0.7 exhibit higher densities before pyrolysis. Pyrolysis has been reported to cause a decrease in density due to the evaporation of elements under high-temperature conditions, leading to the contraction of carbon coin dimensions [28]. $ZnCl_2$ can exit the carbon matrix as vapor, according to the following reaction equation:

$ZnCl_2(s) \rightarrow ZnCl_2(l) \rightarrow ZnCl_2(g)$ (at T > 732°C).

However, Zn can exist in a very stable bond as the metal compound ZnO, according to the following equation:

$ZnCl_2 + H_2O/O^* \rightarrow ZnO(s) + 2HCl(g)/Cl_2(g)$, T ≤ 900°C.

The formed ZnO can be reduced by carbon, T = 907°C.

$ZnO(s) + C(s) \rightarrow Zn(g) + CO(g)$.

The RSL@PC-0.5 sample exhibited an optimal density reduction of 26.43%, leading to a porous carbon (PC) structure with a solid nanostructure and a well-developed pore network, which maximized the SSA [29]. However, in RSL@PC-0.7, excessive catalyst concentration caused an even greater density reduction of 39.31%. This excessive shrinkage was associated with the formation of a larger number of open pores. Beyond a certain threshold, excessive density reduction led to pore wall damage due to hydroxylation, causing pore blockage and preventing electrolyte ions from efficiently accessing the pores of RSL@PC-0.7. This led to the formation of pores that were either too small or too large, reducing the number of active sites and negatively impacting the specific capacitance. The results correlated with previous studies on *Cymbopogon citratus* leaves [30] and the green stem of cassava [31], indicating that specific capacitance was influenced by factors beyond density reduction alone.

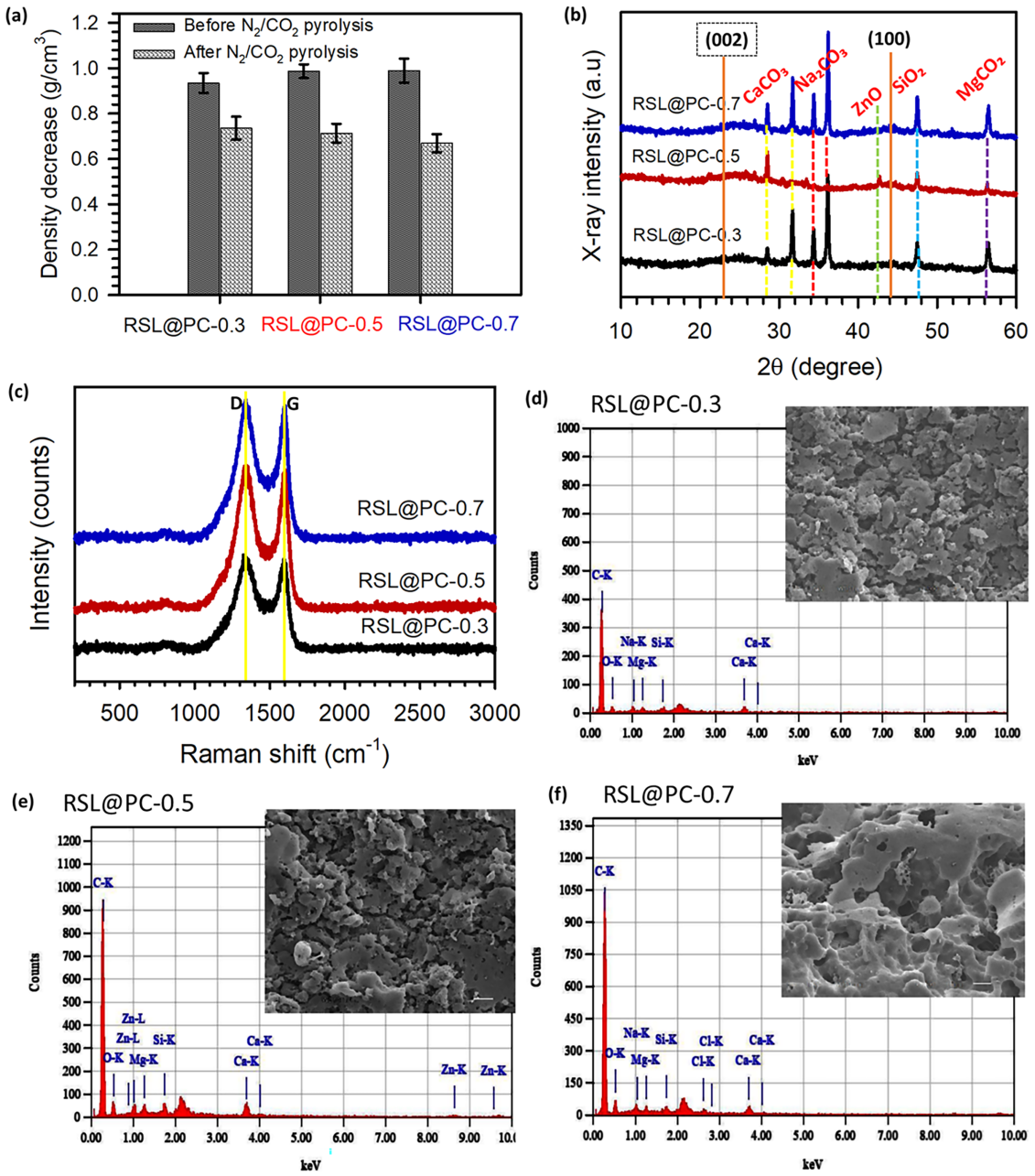

Figure 2: (**a**) Decrease in carbon coin density, (**b**) X-ray diffraction curve, (**c**) Raman spectrum, and (**d**–**f**) carbon elemental composition of RSL@PC-(x).

3.2 Structural Properties

The crystal structure and defects of RSL@PC(x) were investigated using XRD, as shown in Fig. 2b. The results showed an amorphous carbon structure with some graphitic characteristics. This was evidenced by peak broadening at (002) and (100) diffraction angles (24.8° and 45.3°), consistent with JCPDS No. 75–1621. As additional data, the XRD spectral parameters are reported in detail in Table 1, where these results are in good agreement with the data referring to the characteristics of amorphous carbon. The almost flat diffraction peak at 45.3° confirmed a low degree of graphitization, indicating a random atomic

arrangement. The RSL@PC-0.5 sample exhibited the most significant intensity reduction, suggesting a higher degree of porosity and a more disordered carbon structure, confirming its improved amorphous nature with wider diffraction peaks at half-maximum intensity (FWHM = 0.105° and 0.182°). Additionally, all variations displayed distinct peaks at 29°, 38°, and 57°, corresponding to calcium carbonate ($CaCO_3$) (JCPDS No. 47–1743), amorphous silica (SiO_2) (JCPDS No. 46–1045), and magnesium carbonate ($MgCO_3$) (JCPDS No. 25–0526). These compounds were identified as natural elements present in RSL aromatic waste. The combination of carbon and amorphous silica had been reported to enhance the hydrophobic properties of conductor materials while improving the hydrophilic properties of insulating materials [32]. This characteristic was beneficial for improving the electrical conductivity and wettability of RSL@PC(x) when used as an electrode material with superior physicochemical and electrochemical properties. For thinner layers Lc, it can provide increased surface pores in each microcrystalline layer, resulting in activated carbon with a higher surface area. Meanwhile, high La values confirm structural defects in the carbon layer in greater numbers horizontally.

Table 1: XRD measurement data based on lattice parameters from RSL@PC.

Sample	$2\theta_{002}$ (°)	$2\theta_{100}$ (°)	d_{002} (Å)	d_{100} (Å)	L_c (Å)	L_a (Å)
RSL@PC-0.3	25.232	45.796	3.526	1.979	10.956	17.401
RSL@PC-0.5	24.849	45.335	3.580	1.998	6.635	8.893
RSL@PC-0.7	25.602	45.040	3.476	2.012	9.425	12.875

Remarkably, variations in $ZnCl_2$ concentration (0.3 or 0.7 M) led to the absence of detectable zinc compounds in RSL@PC-0.3 and RSL@PC-0.7. This was indicated by a sharper intensity in RSL@PC-0.5 around 44.4°, confirming the presence of zinc oxide (ZnO) (JCPDS No. 36-1451). The loss of Zn in RSL@PC-0.3 and RSL@PC-0.7 is caused by the very low and too much $ZnCl_2$ concentration, resulting in the Zn atoms experiencing complete evaporation during pyrolysis in the form of $ZnCl_2$ compounds. The discovery of Zn atoms in RSL@PC-0.5 is due to the Zn atoms being able to interact with O atoms to form stable bonds of O and Zn nanoparticles, which provide advantages such as increasing specific capacitance through the pseudocapacitance effect and encouraging the formation of more regular pore channels [33].

Structural defects and the level of amorphous content in the PC-RSL(x) samples were analyzed using Raman spectroscopy, as shown in Fig. 2c. The results revealed two distinct peaks corresponding to the D-band (~1350 cm^{-1}) and G-band (~1590 cm^{-1}). An increase in G-band intensity indicated improved material conductivity, associated with a higher carbon content. Meanwhile, the highest D-band intensity was observed in RSL@PC-0.5, suggesting a large SSA and high porosity, as previously reported for bamboo-derived carbon [34] and Chinese fir sawdust [35]. The D-band peak typically arises due to structural irregularities in sp^3-hybridized carbon, which binds to oxygen functional groups and heteroatoms such as O, N, or H. In contrast, the G-band corresponds to the vibration of sp^2-hybridized carbon (C=C) within an aromatic ring structure. A shift in the G-band position toward higher wavenumbers was attributed to changes in heteroatom doping availability [36]. The I_D/I_G ratios of RSL@PC-0.3, RSL@PC-0.5, and RSL@PC-0.7 samples were 1.04, 1.06, and 1.01, respectively. The highest I_D/I_G ratio in RSL@PC-0.5 indicated strong absorption intensity due to its highly disordered carbon structure, which was associated with increased amorphous porosity. Additionally, the broader peak profiles in RSL@PC-0.5 suggested a high degree of amorphous nature, further supporting its superior electrochemical performance.

3.3 Elemental Analysis

The elemental analysis of RSL@PC(x) was conducted using energy-dispersive spectroscopy (EDS) with the energy intensity spectrum of the elements shown in Fig. 2d–f and confirmed in detail in Table 2. Each chemical element in the RSL@PC material exhibited a different energy density. All samples showed a dominance of carbon content (above 85%). Oxygen, magnesium, silica, and calcium were also detected in all samples, originating from the natural elements composing the biomass. The optimal $ZnCl_2$ treatment in TSR@PC-0.5 led to a reduction of carbon content to 86.60% and the complete loss of sodium (0%). Additionally, the appearance of 3.87% Zn and an increase in organic oxygen to 4.26% were observed as key advantages of RSL@PC-0.5. These results indicated that a significant amount of O and Zn heteroatoms had been successfully retained and enhanced after undergoing N_2-CO_2 pyrolysis. The O and Zn elements contributed to additional pseudocapacitance effects, increasing the real capacitance value. The presence of these heteroatoms facilitated the distribution rate of electrolyte ions within the electrode pores [37]. The detection confirmed the successful incorporation of O and Zn into the carbon matrix of RSL@PC-0.5. However, Zn was not detected in the energy spectrum of RSL@PC-0.3 and RSL@PC-0.7 due to the inappropriate catalyst concentration and excessive interaction between Zn and carbon, resulting in levels below the detection limit of the instrument.

Table 2: Composition of elements of RSL@PC(x)-based carbon electrodes.

Sample	Elemental Content (%)							
	C	O	Na	Mg	Si	Ca	Zn	Cl
TSR@PC-0.3	90.99	3.21	0.61	0.83	0.97	3.40	–	–
TSR@PC-0.5	86.60	4.26	–	0.88	1.32	3.08	3.87	–
TSR@PC-0.5	93.00	2.32	0.46	0.68	0.73	2.21	–	0.59

3.4 Surface Area Analysis

The relationship between the pore structure and electrochemical performance of RSL@PC(x) was analyzed by examining the SSA, pore volume, and pore size distribution. The BET analysis results were summarized in Fig. 3, which presented the isotherm curves of RSL@PC-0.3, RSL@PC-0.5, and RSL@PC-0.7. These isotherms exhibit combined characteristics of type I and IV, indicating the interconnectivity of micro-mesopores in the prepared electrodes, see Fig. 3a–c. The variation in $ZnCl_2$ concentration also played a significant role in the formation of active pores. At 0.3 M $ZnCl_2$, the reaction rate of PC formation was insufficient, leading to suboptimal pore development and a lower surface area. The results correlated with the principle that an optimal level of an activating agent was required to maximize the yield of porous structures [38]. At 0.5 M $ZnCl_2$, the activation process led to a higher number of micropores, accompanied by balanced mesopore growth that enhanced electrode performance. The appropriate amount of $ZnCl_2$ also reinforced the pore structure, making it more robust [39]. The analysis confirmed that RSL@PC-0.5 achieved the highest adsorption isotherm (SSA = 495.31 m^2/g) with a total pore volume of 0.31 cm^3/g. The dominant micropore fraction, exceeding 75%, contributed significantly to the increase in SSA. This surface area was generated by nanostructured pores resembling taproots covered with nano-sized fibers, which significantly enhanced ion diffusion within the RSL@PC-0.5 electrode.

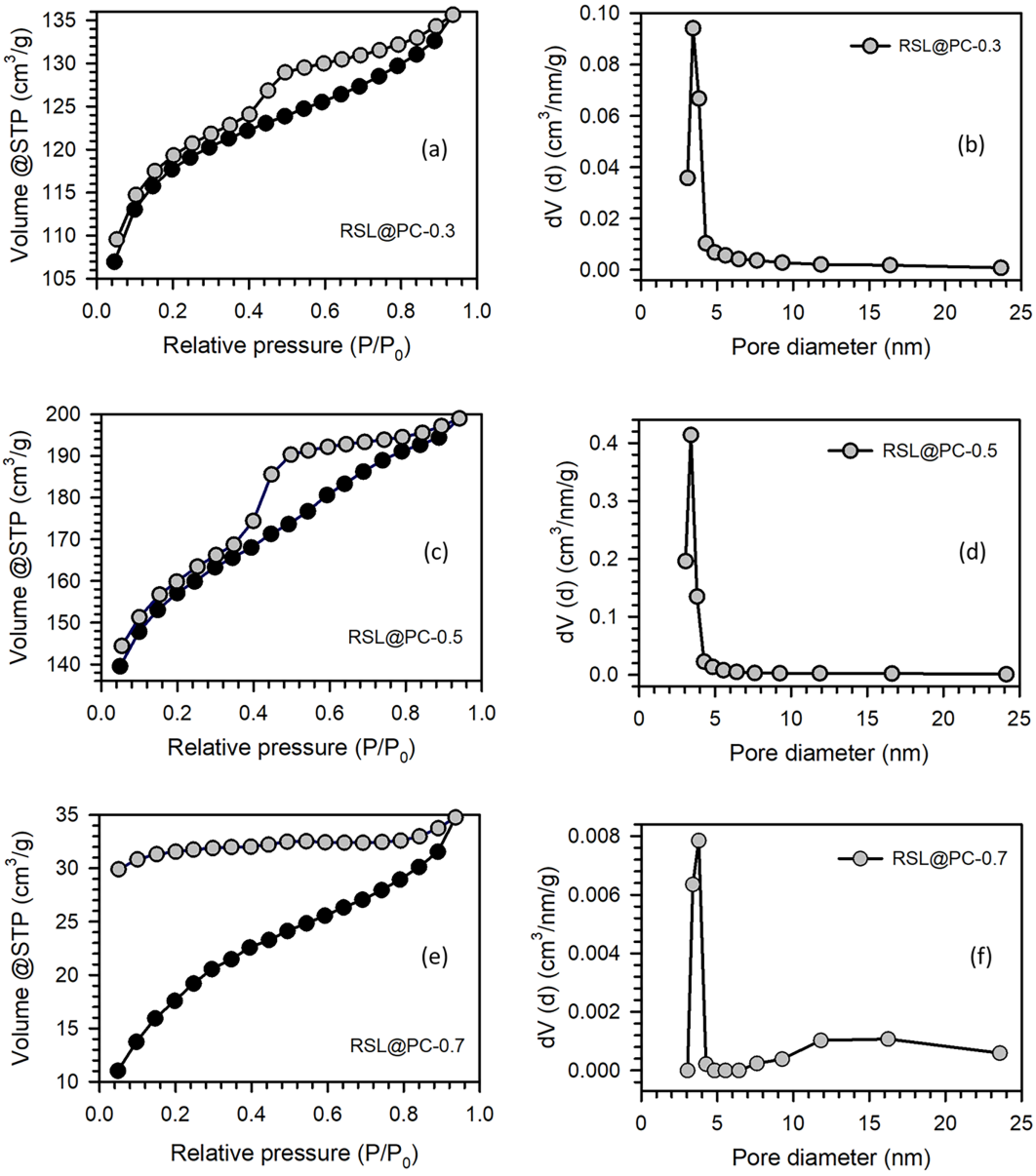

Figure 3: N_2 gas absorption capacity of each RSL@PC-(x) on (**a**–**c**) isotherm curve and (**d**–**f**) pore volume distribution.

In contrast, increasing the $ZnCl_2$ concentration to 0.7 M showed a distorted hysteresis curve (not closed), resulting in a gradual decline in micropore formation. The pore structure is ink-bottle-shaped and features numerous narrow-necked pores. This is because the more intense chemical reaction of $ZnCl_2$ (0.7 M) allows the micropore structure to widen, leading to mesopore formation. The disrupted pore-widening structure results in a loose pore shape resembling the top surface of a bottle with a thin pore neck. The unique narrow pore neck shape with a wide inner surface inhibits the escape of N_2 gas, resulting in a characteristic open-loop hysteresis. The open-loop hysteresis curve exhibits the highest pore-widening structure. This large pore structure significantly contributes to favorable electrolyte insertion and rapid ion diffusion in symmetric supercapacitors. This observation was consistent with results from previous studies by Li et al., who investigated Lotus seedpods-based electrodes where maximum micropore availability was

achieved through KOH impregnation [40]. Similarly, Zhang et al. validated these results in the article on caragana biomass, showing that an optimal micropore structure was achieved at an activation temperature of 700°C [41]. The detailed N_2 gas adsorption parameters were summarized in Table 1. Fig. 2d–f further presented the pore size distribution of RSL@PC-0.3, RSL@PC-0.5, and RSL@PC-0.7, confirming the presence of well-defined mesopores in the prepared carbon materials.

3.5 Morphology

The pore morphology of the selected biomass precursor aromatic waste-derived RSL@PC(x) powder was examined using high-resolution (40.000×) secondary electron imaging, as shown in Fig. 4. Different $ZnCl_2$ catalyst treatments influenced the nanostructure development in RSL carbon. Fig. 4a showed that RSL@PC-0.3 exhibited an underdeveloped pore structure, characterized by randomly distributed particle chunks and a small number of nanopores with suboptimal taproot-like fibers. The rougher surface in Fig. 4b indicates the beginning of micropore growth. Fig. 4c showed that the morphology of RSL@PC-0.5 exhibited a more optimized formation of taproot-like nanostructured pores. This morphology was further decorated with interconnected fibers. The uneven distribution of surface particles suggested that RSL@PC-0.5 successfully maintained a robust taproot-like pore structure with a hierarchical arrangement. In addition, the development of surface micropores with a perfect hierarchical combination is seen in Fig. 4d. This advanced structure facilitated ion distribution, enhanced electron transport, and served as a high-capacity storage medium [42]. The robust nanostructure was further reinforced by the presence of silica elements attached to the PC surface. However, suboptimal catalyst conditions led to a decrease in silica content and surface roughness [43]. This analysis was consistent with the EDS results which confirmed the percentage of silica present. The addition of an activator promoted pore development toward an improved structure. However, excessive $ZnCl_2$ activation at a concentration of 0.7 M led to significant pore structure degradation. Fig. 4e showed that the rougher pore walls collapsed, forming a flatter surface. This was consistent with the smoother appearance of PC-RSL-0.7, corresponding to a substantial reduction in pore availability, confirmed in Fig. 4f. The diminished pore structure reduced the effectiveness of the RSL@PC-0.7 electrode. These results correlated with a study by Boonraksa et al. who studied rice husk-derived organic materials [44]. The publication showed that increasing $ZnCl_2$ and KOH activator concentrations could lead to excessive silica deposition on the surface. The study of RSL@PC with fiber-like nanostructures exhibiting a competitive SSA was previously reported using more complex methods as summarized in Table 3. Therefore, the aromatic biomass selected in this study successfully demonstrated nanofiber modification in carbon materials through a strategic combination of biomass selection, $ZnCl_2$ catalyst activation, and high-temperature pyrolysis.

3.6 Electrochemical Properties

The supercapacitor device of the PC-RSL electrode was examined for its capacitive performance through two measurement methods, namely CV and GCD with the participation of various components. The tests were conducted with a two-electrode symmetric system in an acidic 1 M H_2SO_4 aqueous electrolyte. First, the EDLC properties were assessed using the CV method with the measurement results shown in Fig. 5a. The CV curve exhibited a near-rectangular shape with slight distortions, recorded within a potential window of (0-1-0) V and optimized at scan rates of 1, 2, 5, and 10 mV/s (see Fig. 5b–d).

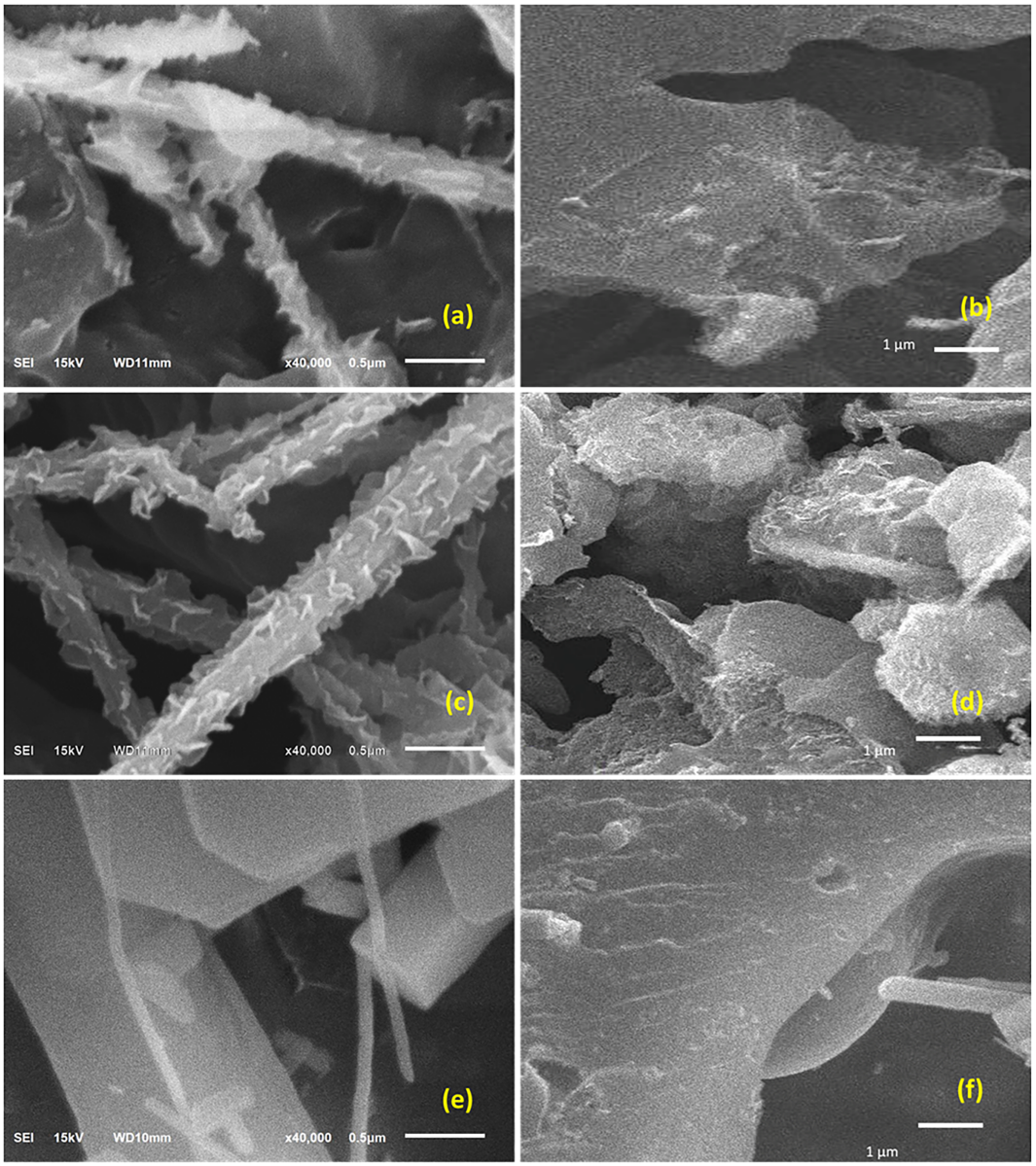

Figure 4: Unique nanostructures such as taproot fibers and hierarchical pore nanostructures view of (**a**,**b**) RSL@PC-0.3, (**c**,**d**) RSL@PC-0.5, and (**e**,**f**) RSL@PC-0.7.

Table 3: SSA of porous carbon nanofibers from various biomasses by different methods.

Precursor	Activator	SSA (m^2/g)	Smic (m^2/g)	Smeso (m^2/g)	V_{tot} (m^3/g)	D_{avg} (nm)	Ref
Manihot esculenta tuber and *Bambusa blumeana* stem	0.06 M $ZnCl_2$	516.29	516.29	–	0.24	1.87	[45]
Gelatin sheets	5 g ZnCl	1152.3	717.5	434.8	0.57	0.72	[46]
Peanut shells	5 g KOH	339.4	–	339.4	0.060	3.505	[47]

(Continued)

Table 3 (continued)

Precursor	Activator	SSA (m^2/g)	Smic (m^2/g)	Smeso (m^2/g)	V_{tot} (m^3/g)	D_{avg} (nm)	Ref
RSL@PC-0.3	0.3 M $ZnCl_2$	365.47	323.389	42.084	0.21	2.30	
RSL@PC-0.5	0.5 M $ZnCl_2$	495.31	373.330	121.977	0.31	2.50	This work
RSL@PC-0.7	0.7 M $ZnCl_2$	67.07	24.105	42.968	0.05	3.22	

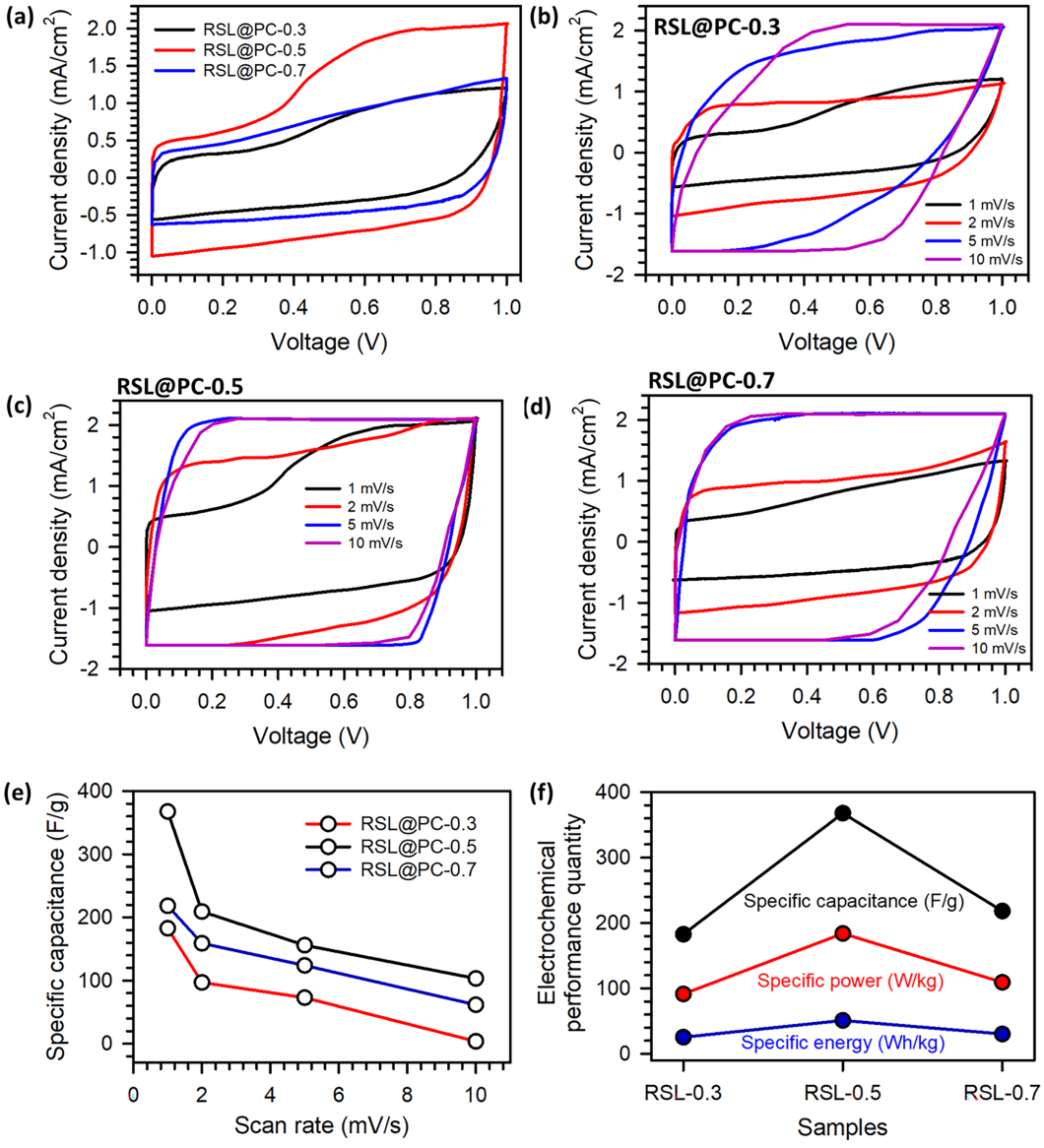

Figure 5: Rectangular curves of voltammetry cycles at scan rates of (**a**) 1 mV/s, scan rates of (1, 2, 5, 10) mV/s at (**b**) RSL@PC-0.3, (**c**) RSL@PC-0.5, and (**d**) RSL@PC-0.7, (**e**) the effect of different scan rates on the specific capacitance values and (**f**) the electrochemical performance of RSL@PC-(x).

The most noticeable deviation in the CV curve appeared in RSL@PC-0.5 due to the presence of pseudocapacitance, attributed to the redox reaction of Zn and O heteroatoms with electrolyte ions [48]. Additionally, the well-developed pore structure of RSL@PC-0.5, particularly the formation of highly conductive mesopores facilitated smooth charge transport and provided a larger storage space. The combination of a taproot-like nanostructure and doping Zn and O significantly enhanced the capacitive performance of the RSL@PC-0.5 electrode. In contrast, RSL@PC-0.3 exhibited a narrower square-shaped CV curve, indicating lower charge storage capacity. This limitation was closely connected to its smaller pore sizes which restricted ion accessibility. The small SSA of RSL@PC-0.3 further contributed to its minimal active site availability. Furthermore, excessive $ZnCl_2$ concentration in RSL@PC-0.7 led to a much narrower CV curve, correlating with reduced electrochemical performance. The micro-mesoporous structure of RSL@PC-0.7 was severely damaged, leading to the formation of macropores. SEM analysis showed that its pore morphology resembled large, damaged aggregates with significantly reduced pore volume which explained the decline in supercapacitor performance [49]. To assess the electrodes' ability to maintain the EDLC properties, scan rates were increased to (2, 5, and 10) mV/s with the results shown in Fig. 5b–d. The CV curves remained rectangular, confirming that each electrode retained its EDLC characteristics even at higher scan rates. However, the scan rate increase led to a decline in electrochemical capacitive performance due to rapid ion movement, which limited effective pore infiltration as indicated in Fig. 5e. Specific capacitance values at 1 mV/s (182, 367, and 218) F/g, at 2 mV/s (97, 209, and 159), at 5 mV/s (73, 155, and 124), and at 10 mV/s (3.8, 103, and 61) F/g for RSL@PC-0.3, RSL@PC-0.5, and RSL@PC-0.7 electrodes with rate capability ranging from 72% to 98%. The capacitive performance of each RSL@PC electrode is further confirmed in Fig. 5f, with the specific energy and specific power corresponding to the increase in specific capacitance.

For more precise electrochemical performance testing, the GCD method was used with the optimization of the results at a current density of 1 A/g. The output of the GCD measurement results showed a symmetrical isosceles triangle curve, confirming that the EDLC was the main contributor to the specific capacitance. The distortion in the measurement curve was caused by the reversible reaction of O and Zn heteroatoms, which caused a bulge in the charging curve [50]. This led to additional real capacitive properties in the EDLC from the pseudocapacitance of the resulting pseudocapacitance. During the activation process of RSL@PC-0.5, chemical interactions occurred between Zn and O to form ZnO compounds distributed on the electrode surface, as a self-doping that was integrated in the carbon framework without a specific external doping process that was redox-active in producing pseudocapacitance, creating hetero-interfaces and defect sites. The length of the charge-discharge time determined the better specific capacitance performance. The diversity of the storage capacity of the RSL@PC electrode was shown in Fig. 6, and its values were summarized in Table 2. Therefore, the study showed that the electrodes prepared with different catalyst levels reasonably affected the electrical storage capacity of the RSL biomass-based supercapacitor even though the power density remained the same. The ability of the RSL@PC-0.5 electrode to maintain its maximum EDLC properties was tested at different current densities (1, 2, and 5 A/g). The EDLC formed at increasing current density, which caused suboptimal ion movement. The distribution time was limited by faster ion movement, leading to a decrease in the specific capacitance of the RSL@PC-0.5 electrode. The RSL@PC-0.5 electrode was able to maintain its EDLC properties at 5 A/g, with the best performance observed at 1 A/g, reaching 490.25 F/g. These results indicated the high electrochemical stability of biomass-based PC materials. The increase in current density caused a decrease in the capacitive performance of the supercapacitor due to the higher charge density, which led to ions moving too quickly [51]. This limited the time available for electrolyte ions to be evenly distributed and fill the electrode pores. The RSL@PC-0.5 sample further showed better capacitive performance in storage capability.

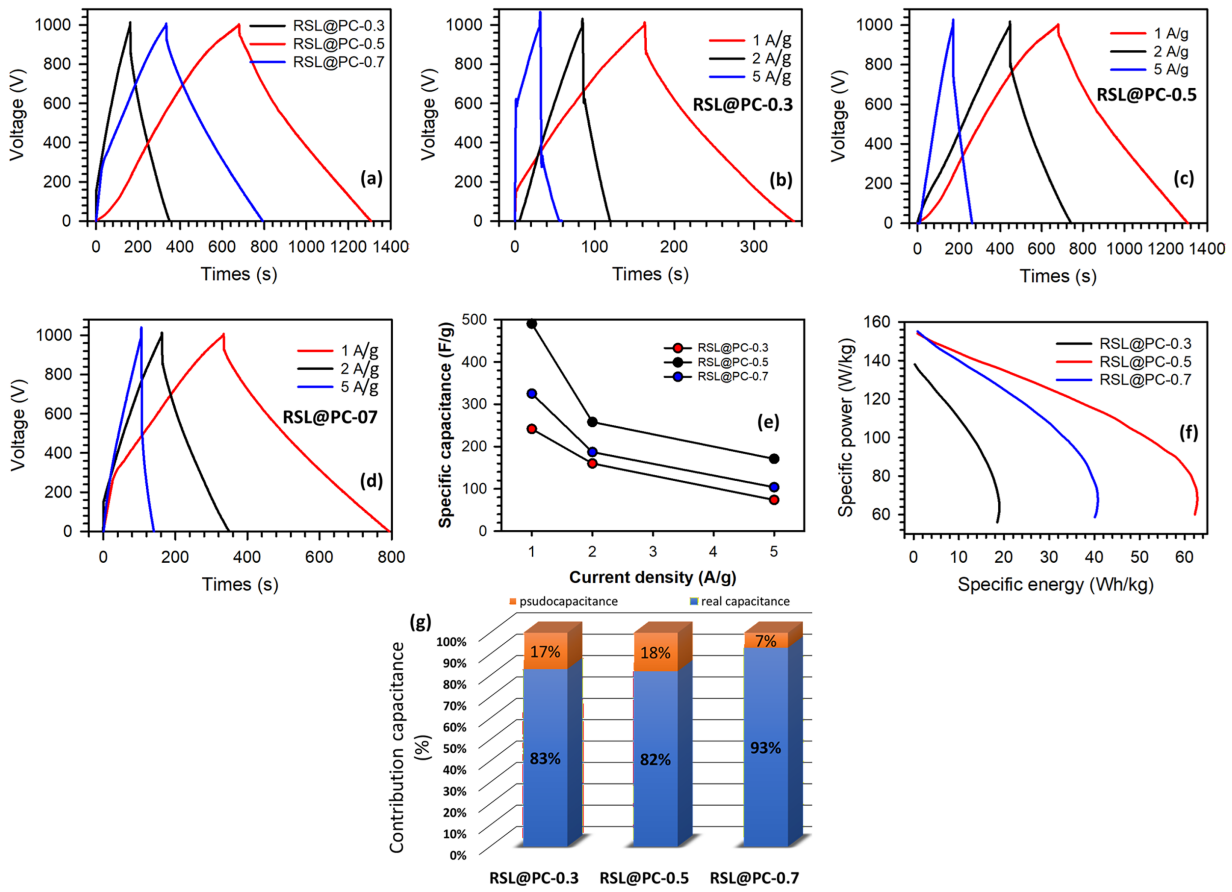

Figure 6: Electrode charge-discharge cycles at current (**a**) 1 A, current (1, 2, 5) A at (**b**) RSL@PC-0.3, (**c**) RSL@PC-0.5, and (**d**) RSL@PC-0.7, (**e**) Csp vs. current density, (**f**) The relationship between specific energy and specific power density, (**g**) specific capacitance contribution of RSL@PC-(x).

The GCD curve of the RSL@PC electrode maintained an isosceles triangular shape at 5 A/g, which confirmed the low internal resistance value due to its high pore volume, nanofiber morphology, and the successful doping of Zn and O [52]. The specific capacitance values for the RSL@PC-0.3, RSL@PC-0.5, and RSL@PC-0.7 samples at 1 A/g (241.63, 490.25, and 325.13 F/g), at 2 A/g (160, 258, and 187 F/g) and at 5 A/g (74, 171, and 104 F/g), with rate capability ranging from 66% to 70%. In addition, changes in the specific capacitance values for each variation of catalyst content at different current densities were shown in Fig. 6b–e. Comparing the three samples, RSL@PC-0.5 contributed the highest specific capacitance supported by the strong porous framework with taproot fibrous structure with maximum SSA and micro-meso volume as sufficient electrolyte ion absorption media [53]. Furthermore, the high electrochemical performance of RSL@PC-0.3, RSL@PC-0.5, and RSL@PC-0.7 materials was studied by evaluating the output energy and power of the as-produced supercapacitors. Through the ragon plot as observed in Fig. 6f, the output energy and power of the three supercapacitor devices were 40.78, 62.93, and 18.93 Wh/kg as well as 155.16, 156.67, 138.42 W/kg, respectively. These performances were comparable to other biomass carbon materials as summarized in Table 4. Finally, the biomass selection (TSR) method followed by the application of $ZnCl_2$ catalyst with high-temperature pyrolysis was proven to produce high-quality carbon materials featuring taproot-like nanofibers and enriched with Zn as well as O heteroatoms, leading to high-performance supercapacitor electrodes. It is clear that, the optimization of the performance of the RSL@AC

electrode is greatly supported by the large contribution of pseudocapacitance, especially at RSL@AC-0.5 up to 18%, as shown in Fig. 6g.

Table 4: Comparison of electrochemical performance of porous carbon electrodes with different precursors, nanostructures, and doping.

Biomass	Nanostructure	Doping	Csp (F/g)	Esp (Wh/kg)	Psp (W/kg)	R (Ω)	Ref
Jute fibers	Popcorn-like	N	503	30.5	250	0.23	[54]
Waste sugarcane bagasse	Fiber	O	364.13	44.07	401.7	–	[55]
Platycladus orientalis leaves	Hierarchical	N, O, S	308.5	17.5	162.5	–	[56]
Zivzik pomegranate peels	Spherical	Zn, O	265.2	7.29	3600	7.12	[57]
Phenolic resin	Coral-like	–	282.8	9.82	115	0.098	[58]
RSL@PC-0.5	Taproot fibers	Zn, O	490	62.93	156.67	0.37	This work

4 Conclusion

In conclusion, the preparation of porous activated carbon taproot fibers from RSL waste with natural heteroatom doping Zn and O was successfully achieved through a simple and useful method, including $ZnCl_2$ impregnation, carbonisation, and physical activation. During the chemical impregnation procedure with different $ZnCl_2$ concentrations (0.3, 0.5, 0.7), M affected the shape of the pore structure, the availability of natural doping, and the electrochemical performance of the supercapacitor. The appearance of the morphology of the RSL@PC-0.5, similar to a fibrous taproot, supported the provision of active sites for the electrode. At the optimal condition of 0.5 M, the total pore volume, the number of pores, and the degree of amorphity of the electrode increased. Furthermore, the quantities of Zn and O elements reached their maximum states. The solid-state symmetric electrode showed an outstanding capability in the aqueous electrolyte environment of 1 M H_2SO_4, reaching 490 F/g at an operating window of 1 V. The highest energy and power output were also recorded in the RSL@PC-0.5 sample, namely 62.93 Wh/kg and 156.67 W/kg. This study showed the potential for increasing the power of EDLC in the practical application of supercapacitors and its potential as a future energy storage device for the stability of the electric grid. The results were supported by efficient and useful preparation methods for advancing renewable energy sources. Therefore, opening up insights into the preparation of worthless organic materials into useful carbon products with excellent porosity and performance was needed for the sustainable energy revolution with transformative energy storage that minimised environmental impact.

Acknowledgement: Not applicable.

Funding Statement: The research was financially supported by First year Project of Riset Konsorsium Unggulan Berdampak (RIKUB) in Kementerian Pendidikan, Kebudayaan, Riset, dan Teknologi, Republic of Indonesia with the title "Optimization of the capacitive performance of green supercapacitors through engineering of potential Indonesian biomass carbon materials as new renewable energy storage." contract No.: 37889/UN19.5.1.3/AL.04/2025.

Author Contributions: Conceptualization, Erman Taer and Rika Taslim; methodology, Isnasyauqiah and Asmarwati; software, Apriwandi; validation, Bidayatul Armynah, Dahlang Tahir and Abrar Ismardi; formal analysis, Indra Wahyudhin Fathona and Memoria Rosi; investigation, Julnaidi; resources, Asmarwati; data curation, Ninis Hadi Haryanti; writing—original draft preparation, Novi Yanti; writing—review and editing, Novi Yanti; visualization, Ida Usman; supervision, Suryajaya; project administration, Erman Taer; funding acquisition, Erman Taer. All authors reviewed and approved the final version of the manuscript.

Availability of Data and Materials: All contained in this article.

Ethics Approval: Not applicable.

Conflicts of Interest: The authors declare no conflicts of interest.

References

1. Saikia BK, Benoy SM, Bora M, Neog D, Bhattacharjya D, Rajbongshi A, et al. Fabrication of pouch cell supercapacitors using abundant coal feedstock and their hybridization with Li-ion battery for e-rickshaw application. J Energy Storage. 2024;78:110312. doi:10.1016/j.est.2023.110312.
2. Rashid Khan H, Latif Ahmad A. Supercapacitors: overcoming current limitations and charting the course for next-generation energy storage. J Ind Eng Chem. 2025;141:46–66. doi:10.1016/j.jiec.2024.07.014.
3. Speranza R, Zaccagnini P, Scalia A, Tresso E, Lamberti A. Pouch-sealing as an effective way to fabricate flexible dye-sensitized solar cells and their integration with supercapacitors. J Power Sources. 2023;583:233581. doi:10.1016/j.jpowsour.2023.233581.
4. Bhattacharjee J, Roy S. A comprehensive review on integrated photo rechargeable batteries-supercapacitors, and their techno-economic feasibility. J Photochem Photobiol. 2025;25:100257. doi:10.1016/j.jpap.2024.100257.
5. Islam M, Hossain MS, Adak B, Rahman MM, Moni KK, Nur ASM, et al. Recent advancements in carbon-based composite materials as electrodes for high-performance supercapacitors. J Energy Storage. 2025;107:114838. doi:10.1016/j.est.2024.114838.
6. Wang H, Guo JE, Gao Z. A novel strategy for improving the activation efficiency of bio-derived porous carbon using transgenic technology for supercapacitors. J Ind Eng Chem. 2024;129:227–34. doi:10.1016/j.jiec.2023.08.036.
7. Khan J, Shakeel N, Alam S, Al-Kahtani AA, Dahshan A, Saleem MI, et al. Unlocking the potential of sulfurized electrode materials for next-generation supercapacitor technology. Int J Hydrogen Energy. 2024;88:1163–85. doi:10.1016/j.ijhydene.2024.09.143.
8. Dissanayake K, Kularatna-Abeywardana D. A review of supercapacitors: materials, technology, challenges, and renewable energy applications. J Energy Storage. 2024;96:112563. doi:10.1016/j.est.2024.112563.
9. Dar MA, Majid SR, Satgunam M, Siva C, Ansari S, Arularasan P, et al. Advancements in Supercapacitor electrodes and perspectives for future energy storage technologies. Int J Hydrogen Energy. 2024;70:10–28. doi:10.1016/j.ijhydene.2024.05.191.
10. Taer E, Effendi NY, Taslim R, Apriwandi A. Interconnected micro-mesoporous carbon nanofiber derived from lemongrass for high symmetric supercapacitor performance. J Mater Res Technol. 2022;19:4721–32. doi:10.1016/j.jmrt.2022.06.167.
11. Deng J, Zhang Q, Lan Y, Luo L, Dai Z, Lin Z, et al. Two-step preparation of hierarchical porous carbon materials derived from tannin for use as an electrode material for supercapacitors. J Renew Mater. 2023;11(6):2631–46. doi:10.32604/jrm.2023.027163.
12. Xie K, Hu Y, Afonaa-Mensah S, Yuan C, Cao B, Wang S, et al. Study on preparation of nitrogen-doped hierarchically porous and high-performance carbon materials from seaweed biomass. J Renew Mater. 2022;10(2):541–60. doi:10.32604/jrm.2022.017911.
13. Yardım Y, Genel İ, Saka C. Enhanced supercapacitor performance of hierarchical mesoporous sulfur-doped carbon particles from biomass waste for energy storage. Int J Hydrogen Energy. 2025;99:383–93. doi:10.1016/j.ijhydene.2024.12.058.
14. Yan B, Zheng J, Feng L, Zhang Q, Zhang C, Ding Y, et al. Pore engineering: structure-capacitance correlations for biomass-derived porous carbon materials. Mater Des. 2023;229:111904. doi:10.1016/j.matdes.2023.111904.
15. Zingare PA, Pande KN, Peshwe DR, Deshmukh AD. Enhancing capacity stability in redox-mediated supercapacitors through biomass selection. Future Batter. 2025;5:100021. doi:10.1016/j.fub.2024.100021.
16. Chen W, Wang H, Lan W, Li D, Zhang A, Liu C. Construction of sugarcane bagasse-derived porous and flexible carbon nanofibers by electrospinning for supercapacitors. Ind Crops Prod. 2021;170:113700. doi:10.1016/j.indcrop.2021.113700.

17. Saxena Y, Gupta A, Devi P, Kumar A. Acid-treated waste sisal fiber derived activated carbon as efficient electrode material for solid-state supercapacitor. Diam Relat Mater. 2024;149:111672. doi:10.1016/j.diamond.2024.111672.
18. Lv Y, Qi C, Bai Y, Li L, Chen S, He Z, et al. One-step self-assembled biomass carbon aerogel/carbon nanotube/cellulose nanofiber composite for supercapacitor flexible electrode. Diam Relat Mater. 2024;149:111530. doi:10.1016/j.diamond.2024.111530.
19. Jing Z, Zou X, Chen C, Qiao M, Wang S, Feng C. Preparation and electrochemical properties of N, S Co-doped paper fiber carbon foam (PFCF) electrode materials for supercapacitors. J Energy Storage. 2025;112:115538. doi:10.1016/j.est.2025.115538.
20. Muddasar M, Culebras M, Collins MN. Lignin and its carbon derivatives: synthesis techniques and their energy storage applications. Mater Today Sustain. 2024;28:100990. doi:10.1016/j.mtsust.2024.100990.
21. Muddasar M, Beaucamp A, Culebras M, Collins MN. High performance all lignin derived supercapacitors for energy storage applications. Mater Today Sustain. 2024;26:100767. doi:10.1016/j.mtsust.2024.100767.
22. Lobato-Peralta DR, Okolie JA, Orugba HO, Arias DM, Sebastian PJ, Okoye PU. Evaluating the impact of pre-carbonization on activated carbon production from animal-origin precursors for supercapacitor electrode applications. Biomass Bioenergy. 2025;193:107574. doi:10.1016/j.biombioe.2024.107574.
23. Liu S, Dong K, Guo F, Wang J, Tang B, Kong L, et al. Facile and green synthesis of biomass-derived N, O-doped hierarchical porous carbons for high-performance supercapacitor application. J Anal Appl Pyrolysis. 2024;177:106278. doi:10.1016/j.jaap.2023.106278.
24. Jangra R, Mahendia P, Karakoti M, Sahoo NG, Srivastava A, Sinha OP, et al. $ZnCl_2$-assisted conversion of nitrogen-containing biomass carbon from marigold flower: toward highly porous activated nitrogen-doped carbon for low ESR and enhanced energy density supercapacitors. J Energy Storage. 2024;75:109728. doi:10.1016/j.est.2023.109728.
25. Ansari AA, Lv R, Gai S, Parchur AK, Solanki PR, Archana, et al. ZnO nanostructures–future frontiers in photocatalysis, solar cells, sensing, supercapacitor, fingerprint technologies, toxicity, and clinical diagnostics. Coord Chem Rev. 2024;515:215942. doi:10.1016/j.ccr.2024.215942.
26. Afif A, Rahman SM, Tasfiah Azad A, Zaini J, Islan MA, Azad AK. Advanced materials and technologies for hybrid supercapacitors for energy storage—a review. J Energy Storage. 2019;25:100852. doi:10.1016/j.est.2019.100852.
27. Gao P, Yuan P, Wang S, Shi Q, Zhang C, Shi G, et al. Preparation and comparison of polyaniline composites with lotus leaf-derived carbon and lotus petiole-derived carbon for supercapacitor applications. Electrochim Acta. 2024;486:144112. doi:10.1016/j.electacta.2024.144112.
28. Jin P, Wei H, Liu Y, He Z, Zhang Y, Zhang S, et al. Preparation of supercapacitor electrode materials from activated coal liquefaction residue. Int J Electrochem Sci. 2024;19(1):100459. doi:10.1016/j.ijoes.2023.100459.
29. Boulanger N, Talyzin AV, Xiong S, Hultberg M, Grimm A. High surface area activated carbon prepared from wood-based spent mushroom substrate for supercapacitors and water treatment. Colloids Surf A Physicochem Eng Asp. 2024;680:132684. doi:10.1016/j.colsurfa.2023.132684.
30. Taer E, Yanti N, Apriwandi A, Ismardi A, Taslim R. Novel O, P, S self-doped with 3D hierarchy porous carbon from aromatic agricultural waste via H_3PO_4 activation for supercapacitor electrodes. Diam Relat Mater. 2023;140:110415. doi:10.1016/j.diamond.2023.110415.
31. Taer E, Yanti N, Mustika WS, Apriwandi A, Taslim R, Agustino A. Porous activated carbon monolith with nanosheet/nanofiber structure derived from the green stem of cassava for supercapacitor application. Int J Energy Res. 2020;44(13):10192–205. doi:10.1002/er.5639.
32. He D, Gao Y, Wang Z, Yao Y, Wu L, Zhang J, et al. One-step green fabrication of hierarchically porous hollow carbon nanospheres (HCNSs) from raw biomass: formation mechanisms and supercapacitor applications. J Colloid Interface Sci. 2021;581(Pt A):238–50. doi:10.1016/j.jcis.2020.07.118.
33. Wang J, Xu Y, Yan M, Ren B, Dong X, Miao J, et al. Preparation and application of biomass-based porous carbon with S, N, Zn, and Fe heteroatoms loading for use in supercapacitors. Biomass Bioenergy. 2022;156:106301. doi:10.1016/j.biombioe.2021.106301.
34. Yue W, Yu Z, Zhang X, Liu H, Zhang Y, Ma X. Preparation of natural N/O/S Co-doped biomass-derived carbon materials for supercapacitors using multistage gas self-exfoliation effect. J Anal Appl Pyrolysis. 2024;179:106525. doi:10.1016/j.jaap.2024.106525.

35. Yang X, Wang X, Lu B, Huang B, Xia Y, Lin G, et al. Biomass-derived N, S co-doped activated carbon-polyaniline nanorod composite electrodes for high-performance supercapacitors. Appl Surf Sci. 2023;639:158191. doi:10.1016/j.apsusc.2023.158191.
36. Tan F, Wang B, Li X, Xu J, Lu F, Wang X, et al. Biomass-derived carbon nanofibers and electrolytes: toward high-performance lignin-based supercapacitors with enhanced electrochemical performance. Ind Crops Prod. 2025;224:120381. doi:10.1016/j.indcrop.2024.120381.
37. Chai AW, Wang CC, Chen CY. Synthesis and characterization of modified centrifuged-electrospun carbon nanofibers for high-performance supercapacitor electrodes. J Taiwan Inst Chem Eng. 2024;156:105329. doi:10.1016/j.jtice.2023.105329.
38. Chen Z, Chen Y, Wang Q, Yang T, Luo Q, Gu K, et al. Molecularly-regulating oxygen-containing functional groups of ramie activated carbon for high-performance supercapacitors. J Colloid Interface Sci. 2024;665:772–9. doi:10.1016/j.jcis.2024.03.177.
39. Lu S, Xiao Q, Yang W, Wang X, Guo T, Xie Q, et al. Multi-heteroatom-doped porous carbon with high surface adsorption energy of potassium derived from biomass waste for high-performance supercapacitors. Int J Biol Macromol. 2024;258(Pt 1):128794. doi:10.1016/j.ijbiomac.2023.128794.
40. Li Y, Mei J, Wu L, Xu Q, Li Z. Ultrahigh surface area hierarchical porous carbon derived from biomass via a new KOH activation strategy for high-performance supercapacitor. Int J Hydrogen Energy. 2024;49:67–80. doi:10.1016/j.ijhydene.2023.10.319.
41. Zhang ZW, Lu CY, Liu GH, Cao YJ, Wang Z, Yang TT, et al. Self-assembly of caragana-based nanomaterials into multiple heteroatom-doped 3D-interconnected porous carbon for advanced supercapacitors. Mater Today Adv. 2023;19:100394. doi:10.1016/j.mtadv.2023.100394.
42. Husain A, Ansari K, Mahajan DK, Kandasamy M, Ansari MNM, Giri J, et al. Harnessing sustainable N-doped activated carbon from walnut shells for advanced all-solid-state supercapacitors and targeted Rhodamine B dye adsorption. J Sci Adv Mater Devices. 2024;9(2):100699. doi:10.1016/j.jsamd.2024.100699.
43. Pimsawat A, Tangtrakarn A, Pimsawat N, Khamkongkaeo A, Daengsakul S. Super activated carbon-silica composite from silkworm excrement by microwave-assisted KOH activation for adsorption and supercapacitor. Environ Technol Innov. 2025;37:104034. doi:10.1016/j.eti.2025.104034.
44. Boonraksa N, Swatsitang E, Wongsaprom K. Biomass nanoarchitectonics with activated rice husk char for nanoporous carbon as electrode material: enhancing supercapacitor electrochemical performance. J Non Cryst Solids. 2024;637:123064. doi:10.1016/j.jnoncrysol.2024.123064.
45. Diantoro M, Muthi Aturroifah NI, Luthfiyah I, Utomo J, Hamidah I, Yuliarto B, et al. 3D-porous activated carbon morphological modification of *Manihot esculenta* tuber and *Bambusa blumeana* stem for high-power density supercapacitor: biomass waste to sustainable energy. Carbon Resour Convers. 2025;8(4):100313. doi:10.1016/j.crcon.2025.100313.
46. Hou X, Ren P, Tian W, Xue R, Fan B, Ren F, et al. High-performance Zn-ion hybrid supercapacitors based on biomass-derived hierarchical porous carbon through template-activated bifunctional induced and ice-crystal assisted strategy. J Power Sources. 2024;603:234408. doi:10.1016/j.jpowsour.2024.234408.
47. Nithya R, Ananthi V, Raja R, Arun A. Surface engineering via freezing-assisted pretreatment and low-energy pyrolysis for biomass waste-derived activated carbon for MFC application. Biomass Bioenergy. 2026;206:108635. doi:10.1016/j.biombioe.2025.108635.
48. Sielicki K, Maślana K, Mijowska E. Fallen autumn leaves—the source of highly porous carbon for Zn-ion hybrid supercapacitors. Diam Relat Mater. 2024;144:111021. doi:10.1016/j.diamond.2024.111021.
49. Wannasen L, Chanlek N, Mongkolthanaruk W, Daengsakul S, Pinitsoontorn S. Enhancing electrochemical properties of bacterial cellulose-derived carbon nanofibers through physical CO_2 activation. Mater Sci Energy Technol. 2025;8:13–23. doi:10.1016/j.mset.2024.07.005.
50. Taer E, Yanti N, Padang E, Apriwandi A, Zulkarnain Z, Haryanti NH, et al. Aromatic biomass (torch ginger) leaf-derived three-dimensional honeycomb-like carbon to enhance gravimetric supercapacitor. J Sci Food Agric. 2023;103(15):7411–23. doi:10.1002/jsfa.12846.

51. Pourkheirollah H, Vitto RIM, Volperts A, Vindt ST, Grīnberga L, Kučinskis G, et al. Enhancing specific capacitance and energy density in printed supercapacitors: the role of activated wood carbon and electrolyte dynamics. Carbon Trends. 2025;18:100436. doi:10.1016/j.cartre.2024.100436.
52. Xiong C, Zheng C, Zhang Z, Xiong Q, Zhou Q, Li D, et al. Polyaniline@cellulose nanofibers multifunctional composite material for supercapacitors, electromagnetic interference shielding and sensing. J Mater. 2025;11(1):100841. doi:10.1016/j.jmat.2024.01.015.
53. Teng Z, Han K, Wang M, Qi J, Liu J, Li Y. Dual-frequency ultrasonic-assisted enzymolysis for synthesis of microstructure regulated biomass-derived porous carbon for high-performance supercapacitors. Ultrason Sonochem. 2025;112:107213. doi:10.1016/j.ultsonch.2024.107213.
54. Cheng MC, Chang YS, Tsai DC, Huang YL, Shieu FS. High content heteroatoms doped and valuable biomass derived activated carbon composited with graphene for high performance supercapacitors. Fuel. 2025;387:133790. doi:10.1016/j.fuel.2024.133790.
55. Kang Z, Xu D, Zhao L, Liu D. Boosting supercapacitor performance with high-specific surface area porous carbon derived from sugarcane bagasse. J Energy Storage. 2024;104:114718. doi:10.1016/j.est.2024.114718.
56. Chen Y, Tang Q, Shen C, Lei Y, Chen X. Activation-self-activation strategy for one-step preparation of *Platycladus orientalis* leaves based N-O-S self-doping hierarchical porous carbon for high-performance supercapacitor. Ind Crops Prod. 2025;225:120584. doi:10.1016/j.indcrop.2025.120584.
57. Saka C, Levent A. Fabrication of nitrogen and ZnO doped on carbon particles obtained from waste biomass and their use as supercapacitor electrodes for energy storage. Int J Hydrogen Energy. 2024;90:1070–83. doi:10.1016/j.ijhydene.2024.10.061.
58. Ji L, Zhang Y, Li X, Jiao T, Dong X, Zhang R, et al. Coral-like interconnected porous carbon derived from phenolic resin/ammonium alginate composite for high-rate supercapacitor. J Power Sources. 2023;573:232933. doi:10.1016/j.jpowsour.2023.232933.